Supplemental Information

for

Conformal Electrochemical Deposition of Intermetallic AuCu Thin Films for Convergent C-N Coupling

Carter S. Gerke[1†], Gregory D. Y. Foley[1†], Logan M. Wilder[3], Yuwei Yang[4,5], James L. Young[3], Nicholas M. Bedford[4,5,6], Elisa M. Miller[3], V. Sara Thoi[1,2]*

[†]These Authors Contributed Equally

[1] Department of Chemistry, Johns Hopkins University, Baltimore, Maryland 21218, USA.
[2] Department of Materials Science and Engineering, Johns Hopkins University, Baltimore, Maryland 21218, USA.
[3] Chemistry and Nanoscience Center, National Renewable Energy Laboratory, Golden, Colorado 80204, USA.
[4] School of Chemical Engineering, University of New South Wales, Syndey, New South Wales 2052, Australia.
[5]ARC Centre of Excellence in Carbon Science and Innovation, University of New South Wales 2052, Australia.
[6]Department of Chemistry, Colorado School of Mines, Golden, Colorado 80401, USA.

Table of Contents:

*Authors to whom correspondence should be addressed: sarathoi@jhu.edu

Experimental Details:

Instrumentation: The morphology and surface purity of the AuCu foils were characterized using a Hitachi S-4800 SEM, 3.0kV. All electrochemistry measurements were conducted on either Biologic or CHI660 electrochemical workstations. Electrolyte pH was measured using an EchoSense pH meter. High purity water was acquired from an 18.2 mΩ cm^{-2} grade water purification system. GIXRD experiments were performed on a Rigaku DMAX instrument utilizing a Cu source. Uv-Vis analysis was performed using an Agilent Cary spectrophotometer. XPS data was obtained on a Physical Electronics 5000 Versa Probe III using either monochromatic Al Kα radiation (hν = 1486.7 eV). Cu K-edge and Au L_3-edge XAS measurements were performed at the Beamline for Materials Measurement, beamline 6-bm at the National Synchrotron Light Source II of Brookhaven National Laboratory.

Product Analysis.
Nitrite detection. Electrochemically produced NO_2^- was quantified by preparing 0.5 g of sulfanilic acid was dissolved in 90 mL high purity water and 5 mL of acetic acid. Next, 5 mg of n-(1-naphthyl) ethylenediamine dihydrochloride was added and the solution was then filled to a final volume of 100 mL. The electrolyte was combined with the coloring solution with a ratio of 1:4 and was allowed to develop in the dark for 15 min at room temperature. The UV-Vis absorption spectrum was then acquired at 540 nm. The linear fit of this data exhibited good linearity, R^2 = 0.997 (**Figure S30**).

Ammonia detection. Electrochemically generated ammonia was detected following a modified indophenol blue method and was analyzed using UV-Vis spectroscopy. Three separate colorimetric solutions were freshly prepared: (1) 0.4 g NaOH, 0.5 g salicylic acid, and 0.5 g sodium citrate in 10 mL water; (2) 0.305 mL NaClO in 10 mL water; (3) 0.1 g sodium nitroferricyanide hydrate in 10 mL. Sample detection was performed by adding 1 mL of solution from the cathode side of the cell followed by 1 mL of (1), 0.5 mL of (2), and 100 μL of (3). The UV-Vis spectra were taken following color development for 30 min in the dark and characterized at the peak maximum at 655 nm. The linear fit of the obtained calibration curve exhibited good linearity, R^2 = 0.995 (**Figure S30**)

Urea detection. Electrochemical urea production was quantified by derivatization with diacetyl monoxime followed by UV-Vis analysis. The compound that is formed by reacting urea and diacetyl monoxime has an absorbance maximum at 525 nm. Derivatization was achieved by preparing two separate stock solutions. Solution A was prepared by adding 10 mL concentrated phosphoric acid, 30 mL concentrated sulfuric acid, 60 mL high purity water and 10 mg ferric chloride. Solution B was prepared by dissolving 0.5 g diacetyl monoxime and 10 mg of thiosemicarbazide in 100 mL high purity water. The urea containing solution (either a calibration sample or electrolyte post electrolysis) was mixed with solutions A and B in a 1:2:1 ratio (Urea: A: B) and was then heated at 100 °C for 30 minutes. The solutions were allowed to cool to room temperature before UV-Vis analysis. A final calibration curve was obtained from testing Urea stock solutions between the range of 0.0 to 6.0 μg / mL over three independent tests. The linear fit of this data exhibited good linearity, R^2 = 0.998 (**Figure S31**).

^1H NMR detection of Urea. Proton NMR data was collected on a Bruker Avance 400 MHz Instrument with a liquid nitrogen fed cryoprobe. NMR samples were prepared by adjusting the pH of the electrolyte solution with a 2.5 uL aliquot of 1.0 M Na_2CO_3 which was found to be necessary to resolve the urea peak. A calibration curve was obtained through stock solutions of 0, 2, 4 and 8 ug mL^{-1}. The resulting calibration curve showed good linearity $R^2 = 0.999$ (**Figure S32**). To avoid deuterium exchange with urea, the D_2O locking solvent was sequestered using a glass capillary tube. The NMR data was collected using the WATERGATE solvent suppression method with 128 additive scans.

Faradaic efficiency calculation:
Faradaic efficiency was determined with the following equation:

$$FE = \frac{nFz}{Q}$$

Where n, z, F and Q stand for the number of moles produced, number of electrons required for a specific product, the faraday constant (96,485.3 C mol^{-1}), and the total charge passed during electrolysis, respectively.

X-ray Absorption Spectroscopy (XAS).
For all XAS measurements, the AuCu alloys were deposited onto carbon paper electrodes, which provide similar results as the Ti foil electrodes (**Figure S33**). The alloy carbon paper deposits acted as the working electrode within an electrochemical cell fitted with X-ray transparent Kapton windows. The cell also contained a graphite rod counter electrode and Ag/AgCl reference electrode. During in-situ experiments, the cell was filled with 0.1 M KNO_3 and constantly purged with CO_2. In-situ XAS was conducted at OCP, -0.3 V, and -0.5 V controlled by a portable PalmSens potentiostat.

Data was collected from about 200 eV below to 700 eV above the Cu K- and Au L_3-edges. Data reduction, analysis and modeling were conducted using the Demeter XAS software package (Athena and Artemis).[3] Metal foils of either Cu or Au were used to calibrate E_0 and were used as reference standards. Background subtraction and edge step normalization was performed using Athena. EXAFS fits were performed using Artemis. EXAFS spectrum (χ(k)) was weighted with k^2 values. EXAFS modeling of Cu and Au foils determined the S_02 values of 0.90 for Cu and 0.80 for Au, which were used for all subsequent EXAFS calculations. The EXAFS fits were done in R-space. The scattering paths used for each fit were obtained from the Materials Project.[4] For each fit, Cu-Cu and Au-Au coordination was generated from the Cu-Cu and Au-Au scattering of fcc Cu and Au respectively. The Cu-O coordination was generated from the Cu-O scattering of Cu_2O. The Au-Cu and Cu-Au coordination was generated from the Au-Cu and Cu-Au scattering of $AuCu_3$, AuCu, and Au_3Cu, for $Au_{25}Cu_{75}$, $Au_{50}Cu_{50}$, and $Au_{75}Cu_{25}$ thin-films respectively. For each fit the Au L_3-edge and Cu K-edge spectra were fit together by coupling the Au-Cu and Cu-Au path parameters.

X-ray Photoelectron Spectroscopy (XPS).
The XPS and valence band XPS setup was calibrated with Au and/or Cu metal, which was cleaned via Ar-ion sputtering. The raw atomic concentration has a 5% error due to surface inhomogeneities, surface roughness, literature sensitivity values for peak integration, *etc*. The energy uncertainty of XPS and is +/- 0.050 eV.

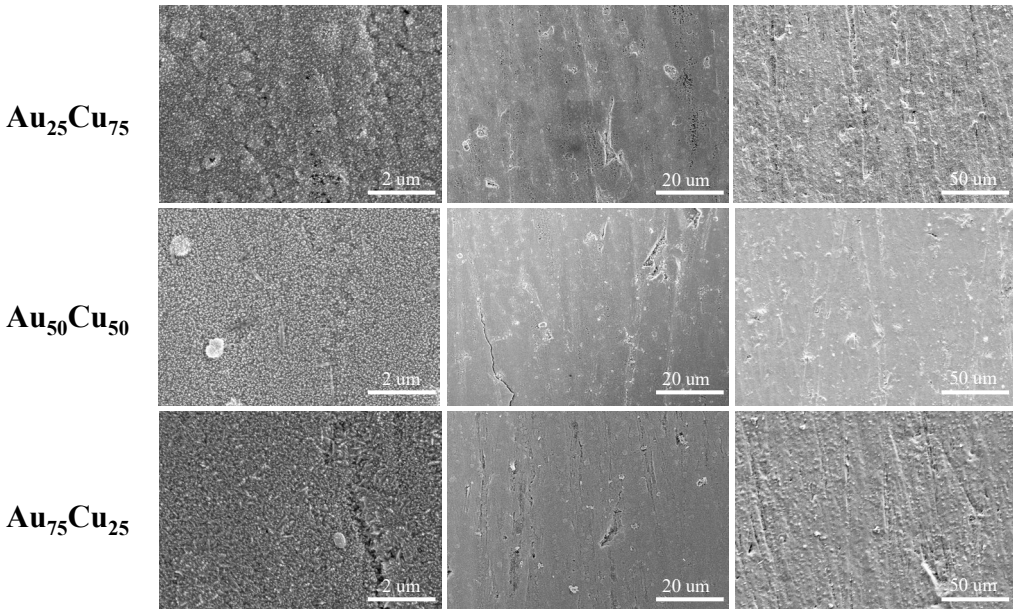

Figure S1: Representative scanning electron micrographs of freshly prepared AuCu alloy electrodes at three magnifications.

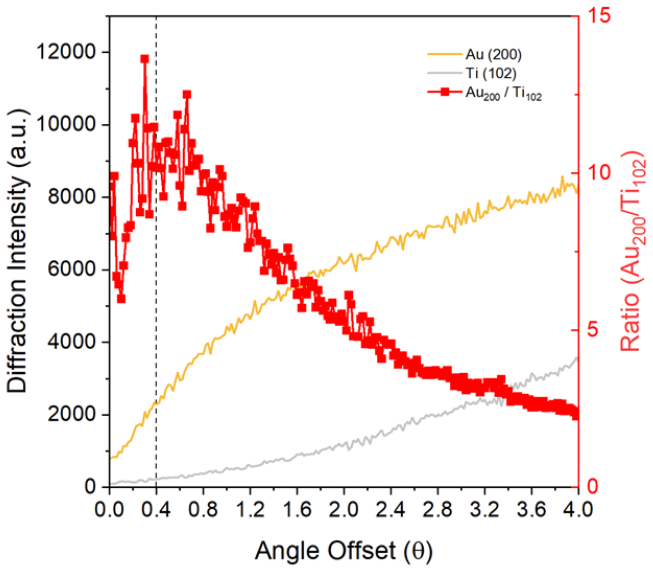

Figure S2. X-ray Diffraction theta plot was used to determine optimum angle offset for GIXRD measurements. For all alloy stoichiometries 0.4° showed to be the optimal angle.

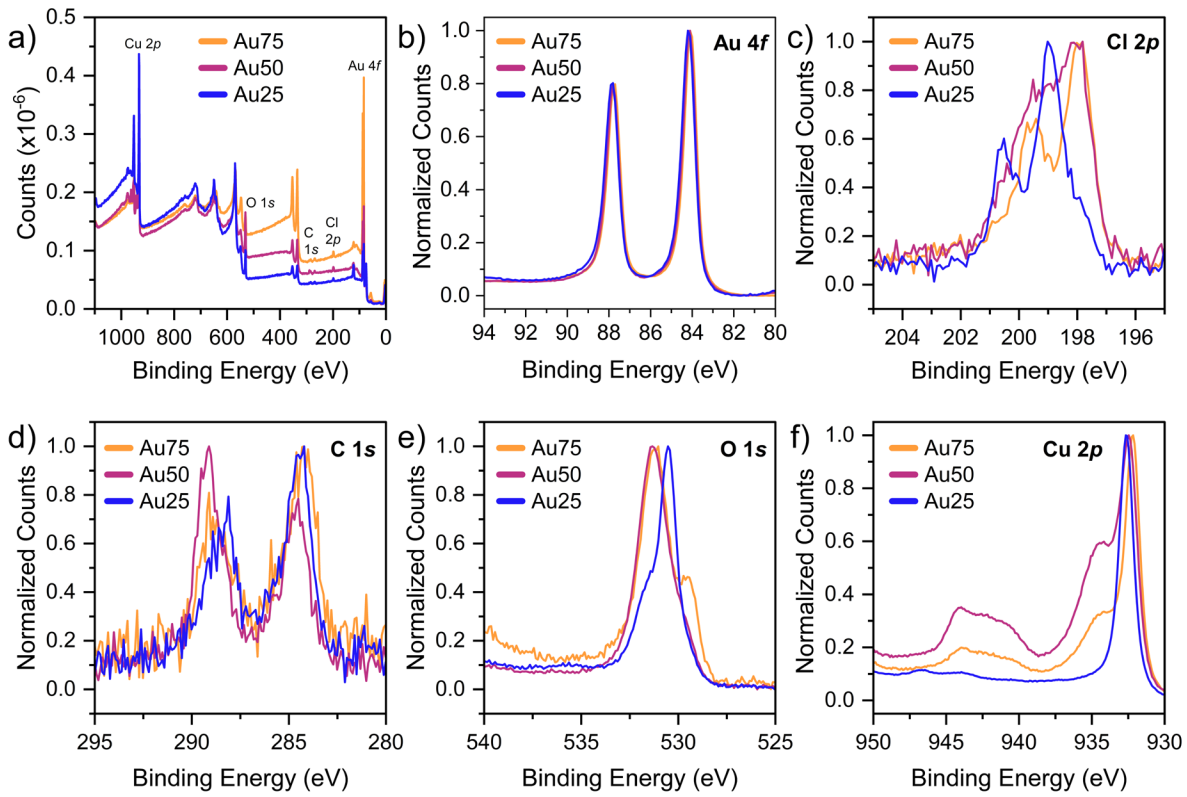

Figure S3: X-ray Photoelectron Spectroscopy of freshly prepared AuCu alloys. (a) XPS survey spectra and high-resolution core level of the (b) Au 4*f*, (c) Cl 2*p*, (d) C 1*s*, (e) O 1*s*, and (f) Cu 2*p* regions.

Table S1. Atomic concentrations of oxygen, gold, and copper by XPS

	O	*Cu*	*Au*	*O* as CuO_x*	*Cu* as CuO_x*	*Cu metal*	*% Cu^0*
$Au_{75}Cu_{25}$	22.49	32.6	31.73	13.10	20.38	12.22	37.5
$Au_{50}Cu_{50}$	39.97	37.5	10.37	15.70	24.20	13.30	35.5
$Au_{25}Cu_{75}$	30.72	50.19	6.88	24.75	49.51	0.68	1.3

Table S2. Surface composition determined by XPS

Sample Identity	% Au in Plating Bath	Atom % Au via XPS	Atom % Cu via XPS
$Au_{75}Cu_{25}$	85	49.3 (70.1)	50.6 (29.8)
$Au_{50}Cu_{50}$	65	21.7	78.3
$Au_{25}Cu_{75}$	27.5	12.1	87.9

* Paratheses denote % surface composition following electrolysis at -0.3V vs. RHE for 1 h.

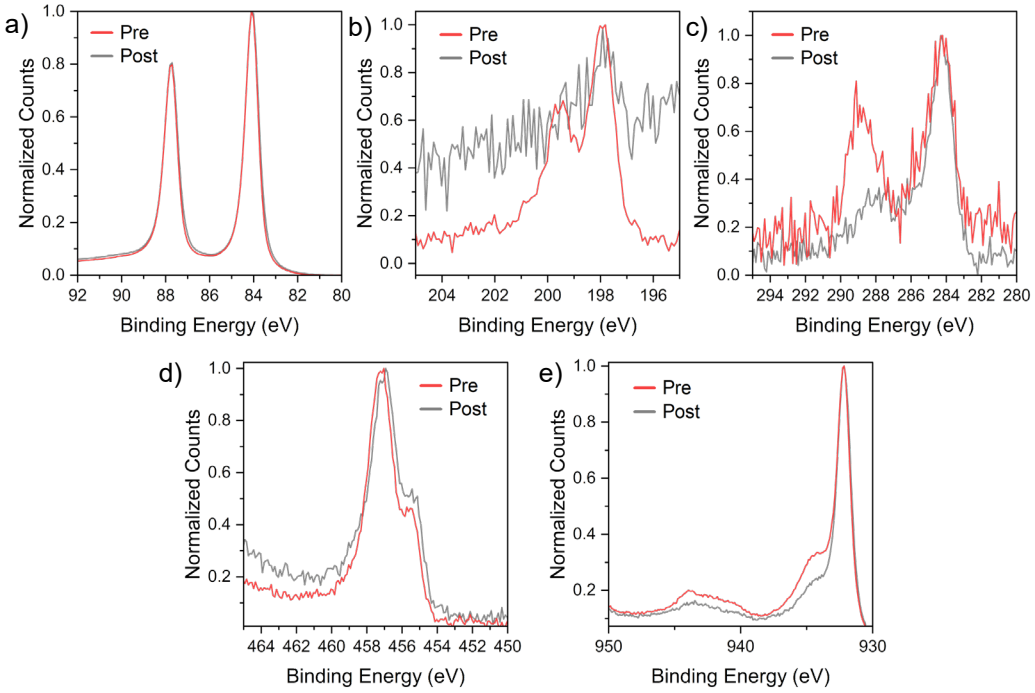

Figure S4. X-ray Photoelectron Spectroscopy of the $Au_{75}Cu_{25}$ alloy pre- and post-electrolysis at -0.3 V vs. RHE. High-resolution core levels of the (a) Au 4*f*, (b) Cl 2*p*, (c) C 1*s*, (d) Ti *2p*, and (e) Cu 2*p*

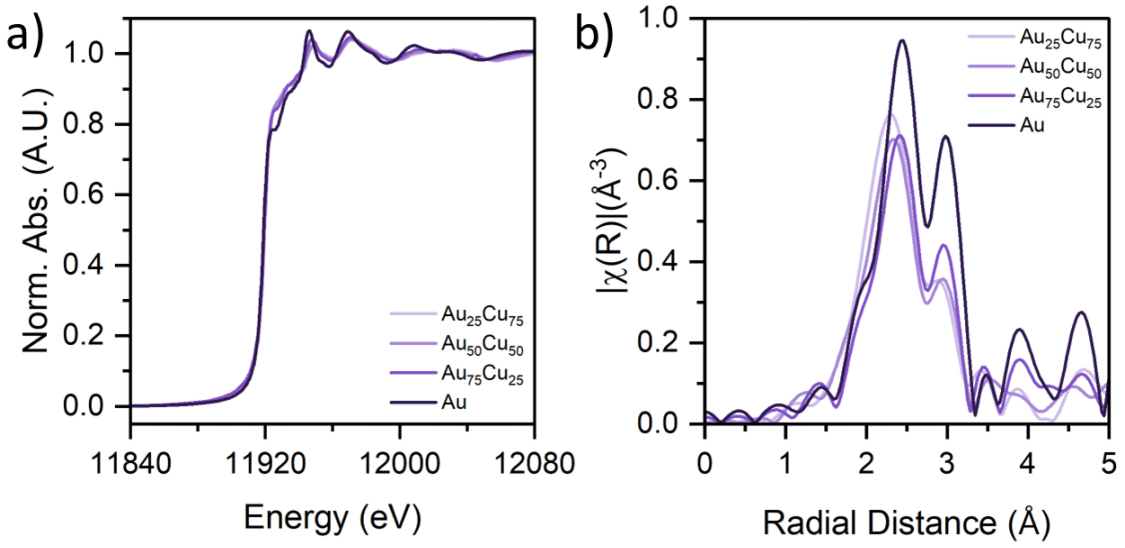

Figure S5. *Ex situ* XAS Au L_3-Edge (a) XANES and (b) EXAFS Spectra for each AuCu alloy electrode in ex-situ. \

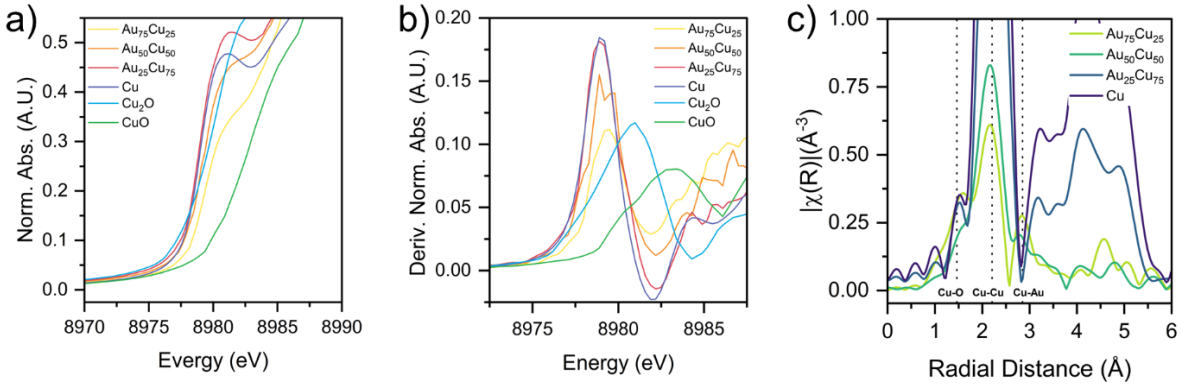

Figure S6. *Ex situ* Cu K-Edge X-ray Absorption Near Edge Structure (XANES) of the intermetallic alloys and Cu, Cu_2O, and CuO standards, (a) normalized energy and (b) derivative normalized energy plots. (c) EXAFS spectra of AuCu alloys with reduced y-axis range to clearly display Cu-Au scattering feature.

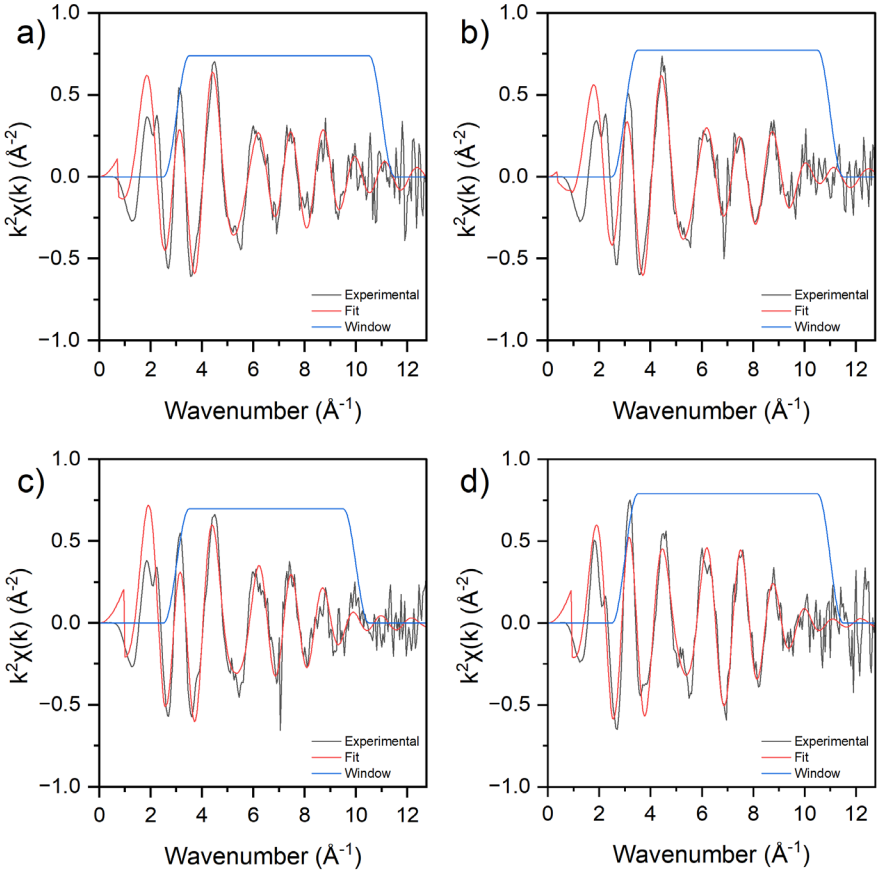

Figure S7. Cu K-Edge EXAFS experimental results (black trace), fittings (red trace) and fitting window (blue trace) in k^2-space for(a) *ex situ* and *in situ* (b) OCP, (d) -0.3 V vs RHE, (d) -0.5 V vs RHE of $Au_{75}Cu_{25}$ in 0.1 M KNO_3, pH = 3.5, under sparging CO_2.

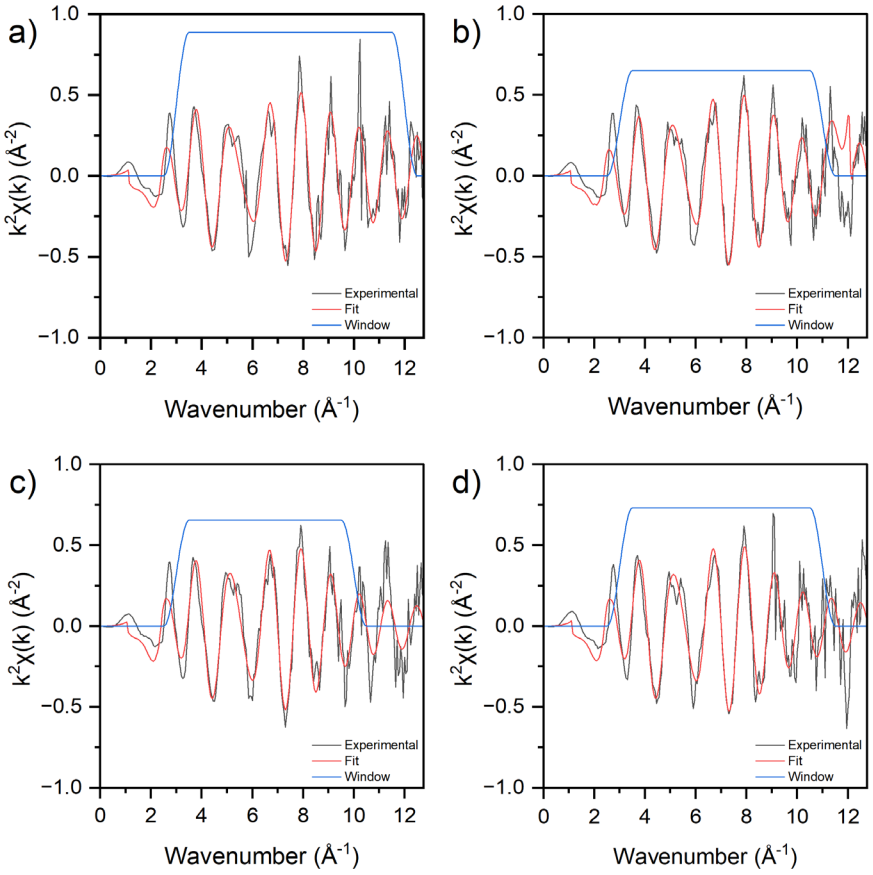

Figure S8. Au L_3-Edge EXAFS experimental results (black trace), fittings (red trace) and fitting window (blue trace) in k^2-space for (a) *ex situ* and *in situ* (b) OCP, (d) -0.3 V vs RHE, (d) -0.5 V vs RHE of $Au_{75}Cu_{25}$ in 0.1 M KNO_3, pH = 3.5, under sparging CO_2.

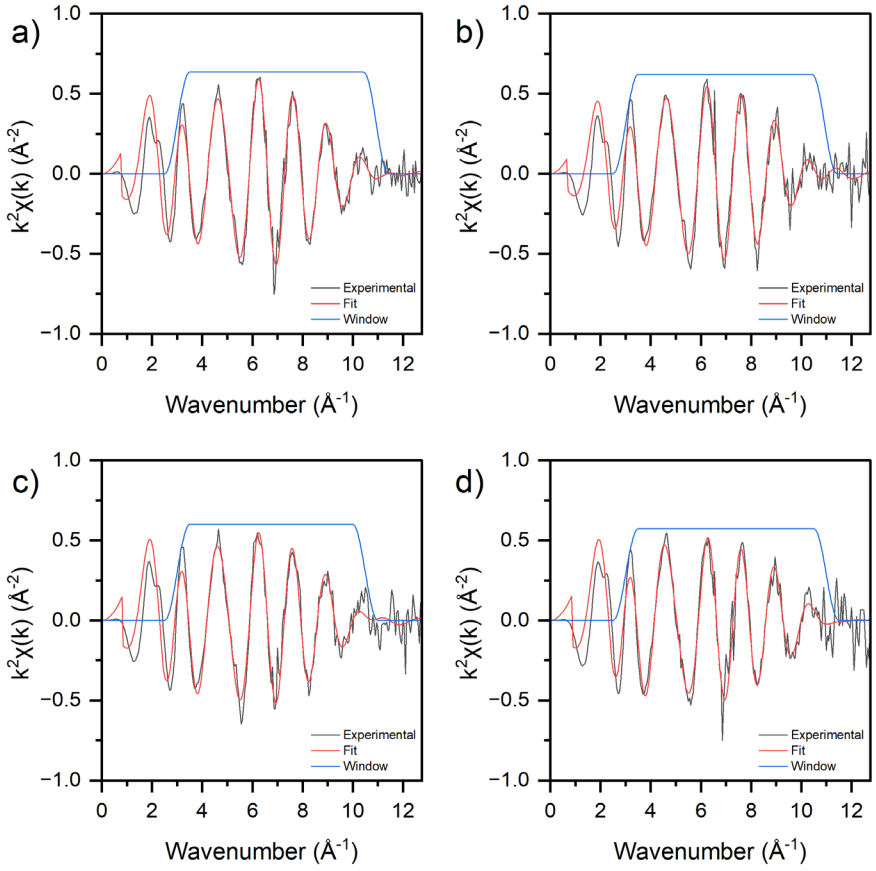

Figure S9. Cu K-Edge EXAFS experimental results (black trace), fittings (red trace) and fitting window (blue trace) in k^2-space for (a) *ex situ* and *in situ* (b) OCP, (d) -0.3 V vs RHE, (d) -0.5 vs RHE of $Au_{50}Cu_{50}$ in 0.1 M KNO_3, pH = 3.5, under sparging CO_2.

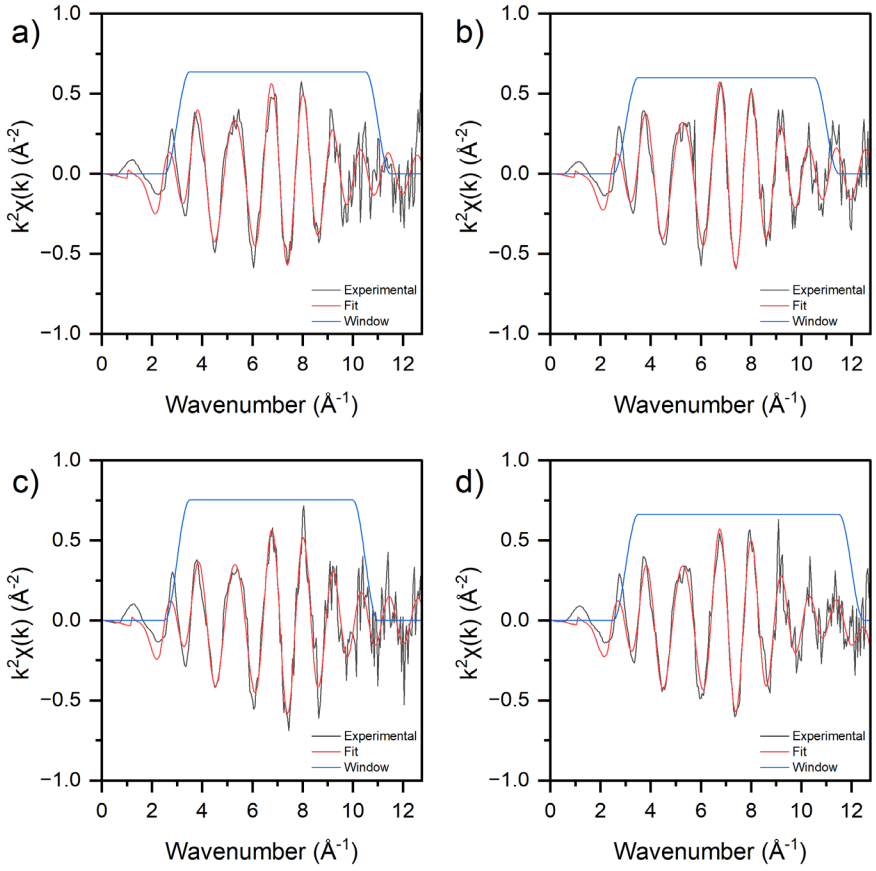

Figure S10. Au L_3-Edge EXAFS experimental results (black trace), fittings (red trace) and fitting window (blue trace) in k^2-space for (a) *ex situ* and *in situ* (b) OCP, (d) -0.3 V vs RHE, (d) -0.5 V vs RHE of $Au_{50}Cu_{50}$ in 0.1 M KNO_3, pH = 3.5, under sparging CO_2.

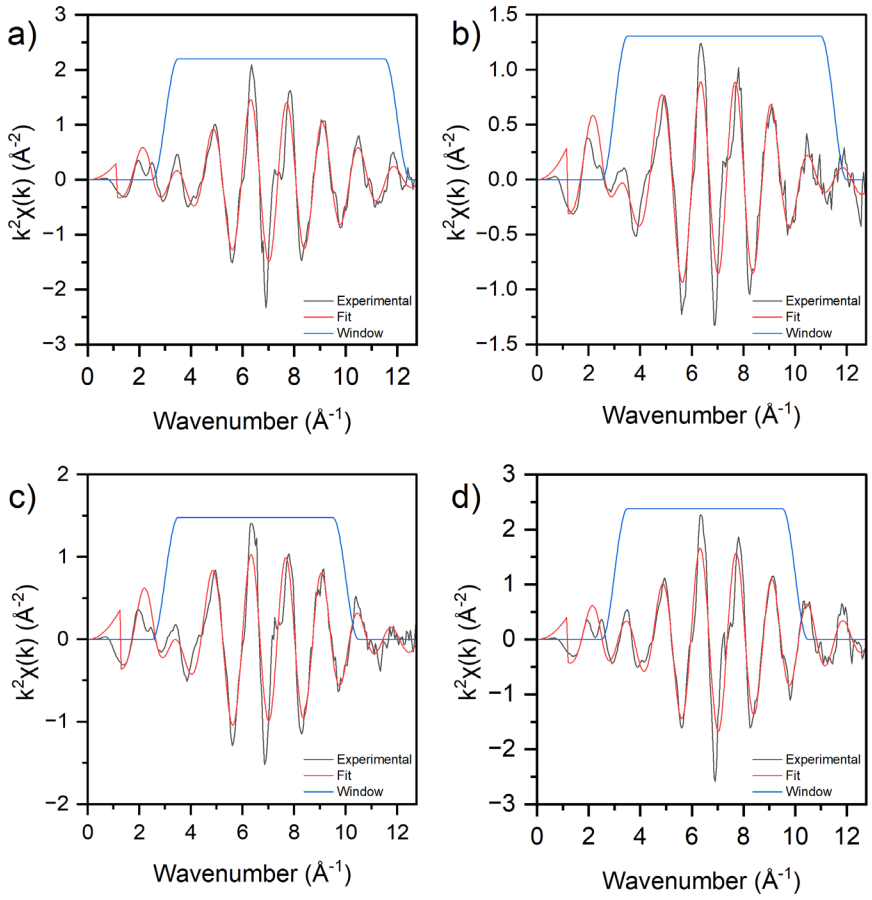

Figure S11. Cu K-Edge EXAFS experimental results (black trace), fittings (red trace) and fitting window (blue trace) in k^2-space for (a) *ex situ* and *in situ* (b) OCP, (d) -0.3 V vs RHE, (d) -0.5 V vs RHE of $Au_{25}Cu_{75}$ in 0.1 M KNO_3, pH = 3.5, under sparging CO_2.

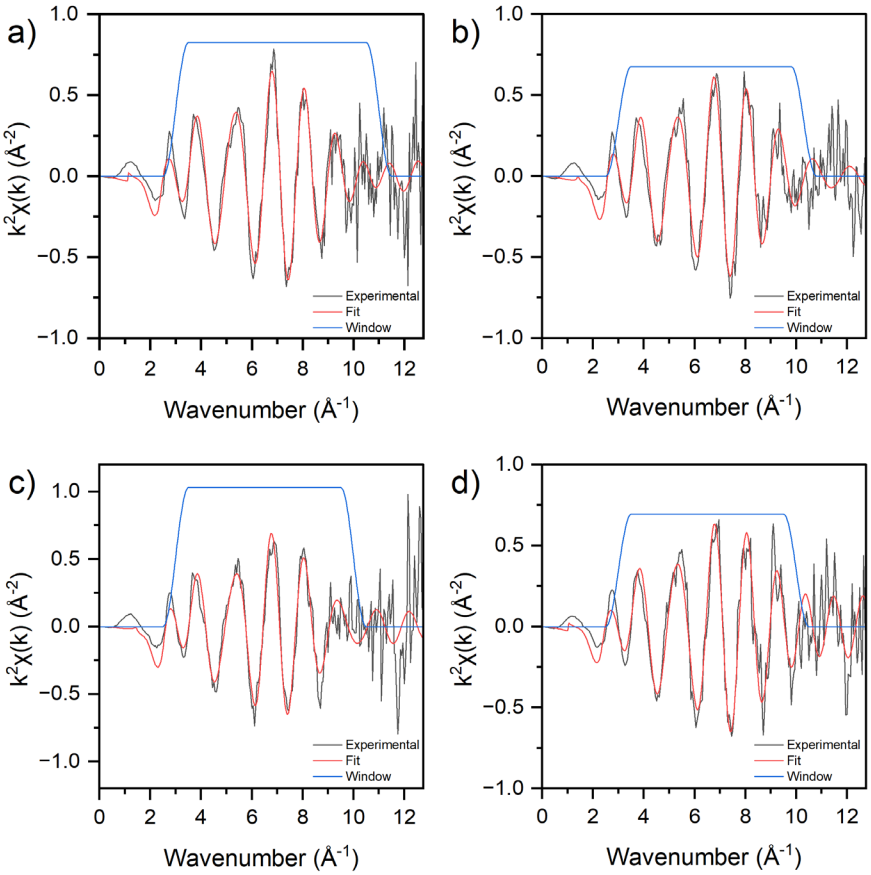

Figure S12. Au L_3-Edge EXAFS experimental results (black trace), fittings (red trace) and fitting window (blue trace) in k^2-space for (a) *ex situ* and *in situ* (b) OCP, (d) -0.3 V vs RHE, (d) -0.5 V vs RHE of $Au_{25}Cu_{75}$ in 0.1 M KNO_3, pH = 3.5, under sparging CO_2.

Table S3. EXAFS fitting results for the $Au_{75}Cu_{25}$ Alloy.

Sample			**Ex-Situ**	**OCV**	**-0.3V**	**-0.5V**
$Au_{75}Cu_{25}$	Coordination number	Au-Au	8.79 ± 0.59	8.92 ± 0.63	9.12 ± 0.72	9.02 ± 0.67
		Au-Cu	0.60 ± 0.78	1.05 ± 0.63	1.72 ± 0.61	1.61 ± 0.62
		Cu-Cu	1.47 ± 0.43	1.05 ± 0.41	0.89 ± 0.44	1.95 ± 0.23
		Cu-Au	5.60 ± 0.71	5.24 ± 0.41	6.02 ± 0.62	5.94 ± 0.32
		Cu-O	0.59 ± 0.09	0.83 ± 0.13	0.95 ± 0.21	0.10 ± 0.08
	Bond length (Å)	Au-Au	2.83 ± 0.01	2.83 ± 0.01	2.83 ± 0.01	2.83 ± 0.01
		Au-Cu	2.67 ± 0.02	2.69 ± 0.02	2.72 ± 0.02	2.71 ± 0.01
		Cu-Cu	2.64 ± 0.02	2.67 ± 0.02	2.58 ± 0.04	2.58 ± 0.01
		Cu-Au	2.67 ± 0.02	2.69 ± 0.02	2.72 ± 0.02	2.71 ± 0.01
		Cu-O	1.89 ± 0.03	1.89 ± 0.02	1.92 ± 0.02	1.98 ± 0.07
	Debye waller factor ($Å^2$)	Au-Au	0.0077	0.0084	0.0061	0.0094
		Au-Cu	0.0155	0.0131	0.0148	0.0145
		Cu-Cu	0.0139	0.0130	0.0133	0.0137
		Cu-Au	0.0155	0.0131	0.0148	0.0145
		Cu-O	0.0035	0.0080	0.0132	0.0045
	R-factor	-	**0.0091**	**0.0170**	**0.0145**	**0.0091**

Table S4. EXAFS fitting results for the $Au_{50}Cu_{50}$ Alloy.

Sample			**Ex-Situ**	**OCV**	**-0.3V**	**-0.5V**
$Au_{50}Cu_{50}$	Coordination number	Au-Au	7.56 ± 1.02	7.03 ± 0.42	6.41 ± 0.97	6.18 ± 0.61
		Au-Cu	3.50 ± 0.56	3.22 ± 0.37	3.70 ± 0.96	3.01 ± 0.50
		Cu-Cu	3.20 ± 0.53	3.00 ± 0.17	3.12 ± 0.23	1.79 ± 0.15
		Cu-Au	3.87 ± 0.31	3.64 ± 0.29	4.10 ± 0.36	4.18 ± 0.33
		Cu-O	0.18 ± 0.13	0.18 ± 0.04	0.21 ± 0.06	0.37 ± 0.06
	Bond length (Å)	Au-Au	2.81 ± 0.01	2.81 ± 0.01	2.80 ± 0.02	2.81 ± 0.01
		Au-Cu	2.67 ± 0.01	2.67 ± 0.01	2.68 ± 0.02	2.68 ± 0.01
		Cu-Cu	2.56 ± 0.00	2.56 ± 0.01	2.56 ± 0.01	2.55 ± 0.01
		Cu-Au	2.67 ± 0.01	2.67 ± 0.01	2.68 ± 0.02	2.68 ± 0.01
		Cu-O	1.88 ± 0.02	1.84 ± 0.02	1.86 ± 0.02	1.88 ± 0.02
	Debye waller factor ($Å^2$)	Au-Au	0.0097	0.0087	0.0086	0.0095
		Au-Cu	0.0146	0.0136	0.0147	0.0136
		Cu-Cu	0.0126	0.0124	0.0136	0.0093
		Cu-Au	0.0146	0.0136	0.0147	0.0136
		Cu-O	0.0009	0.0000	0.0000	0.0025
	R-factor	-	**0.0086**	**0.0036**	**0.0062**	**0.0057**

Table S5. EXAFS fitting results for the $Au_{25}Cu_{75}$ Alloy.

Sample			**Ex-Situ**	**OCV**	**-0.3V**	**-0.5V**
$Au_{25}Cu_{75}$	Coordination number	Au-Au	6.49 ± 1.39	7.58 ± 3.27	8.23 ± 3.06	5.77 ± 1.38
		Au-Cu	4.22 ± 1.00	3.10 ± 1.35	4.45 ± 1.37	4.28 ± 1.88
		Cu-Cu	7.15 ± 0.30	4.42 ± 0.47	5.16 ± 0.43	7.96 ± 0.31
		Cu-Au	1.14 ± 0.74	1.45 ± 0.90	1.31 ± 0.86	1.59 ± 0.97
		Cu-O	0.17 ± 0.11	0.62 ± 0.23	0.49 ± 0.14	0.08 ± 0.09
	Bond length (Å)	Au-Au	2.81 ± 0.02	2.84 ± 0.09	2.87 ± 0.06	2.79 ± 0.03
		Au-Cu	2.66 ± 0.02	2.69 ± 0.02	2.67 ± 0.01	2.67 ± 0.02
		Cu-Cu	2.54 ± 0.01	2.54 ± 0.01	2.55 ± 0.01	2.54 ± 0.01
		Cu-Au	2.66 ± 0.02	2.69 ± 0.02	2.67 ± 0.01	2.67 ± 0.02
		Cu-O	1.84 ± 0.06	1.83 ± 0.03	1.83 ± 0.03	1.41 ± 0.1
	Debye waller factor ($Å^2$)	Au-Au	0.0097	0.0137	0.0130	0.0073
		Au-Cu	0.0123	0.0081	0.0094	0.0140
		Cu-Cu	0.0083	0.0084	0.0085	0.0082
		Cu-Au	0.0123	0.0081	0.0094	0.0140
		Cu-O	0.0000	0.0015	0.0000	0.0030
	R-factor	-	**0.0056**	**0.0306**	**0.0188**	**0.0050**

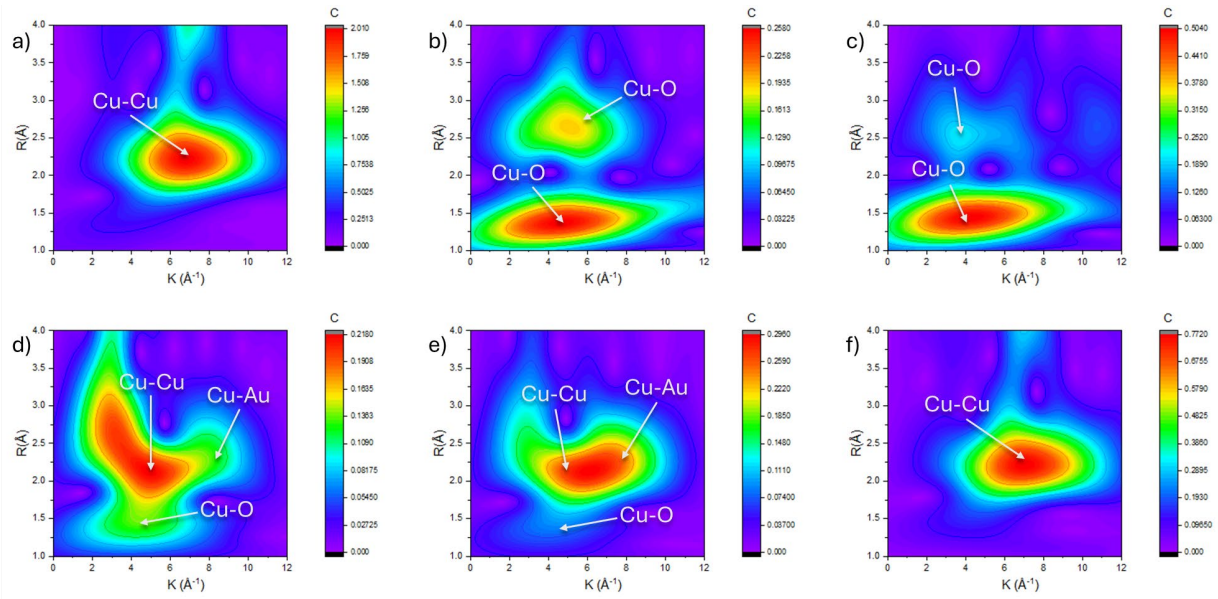

Figure S13. Wavelet transform analysis of Cu K-edge for (a) metallic Cu, (b) Cu_2O, and (c) CuO standards, and (d) $Au_{75}Cu_{25}$, (e) $Au_{50}Cu_{50}$, and (f) $Au_{25}Cu_{75}$ alloys. Wavelet transform lobes corresponding to Cu-Cu, Cu-Au, and Cu-O coordination are labeled.

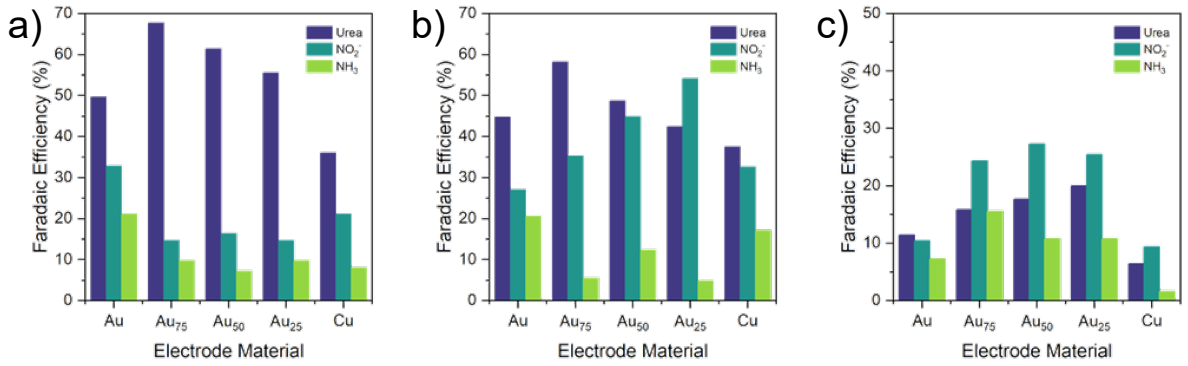

Figure S14. Liquid product distributions following electrolysis of the three AuCu alloys and their parent metals at three different current densities, (a) -250 μA cm^{-2}, (b) -500 μA cm^{-2}, and (c) -1000 μA cm^{-2} in a pH 5 solution of 0.1 M KNO_3 and flowing CO_2.

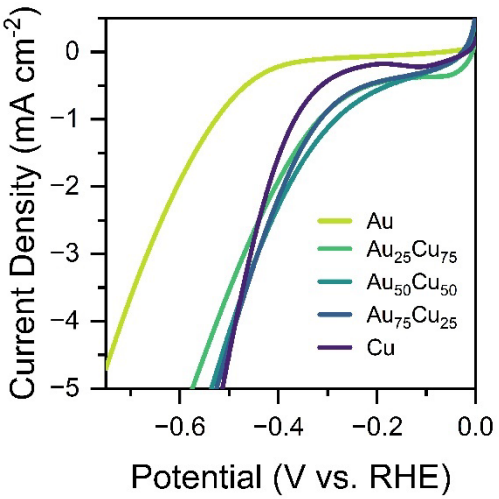

Figure S15. Linear Sweep Voltammograms (LSVs) of each electrode material in CO_2 sparged 0.1 M KNO_3, pH = 3.5. Data was collected in quiescent solutions at 100 mV/s.

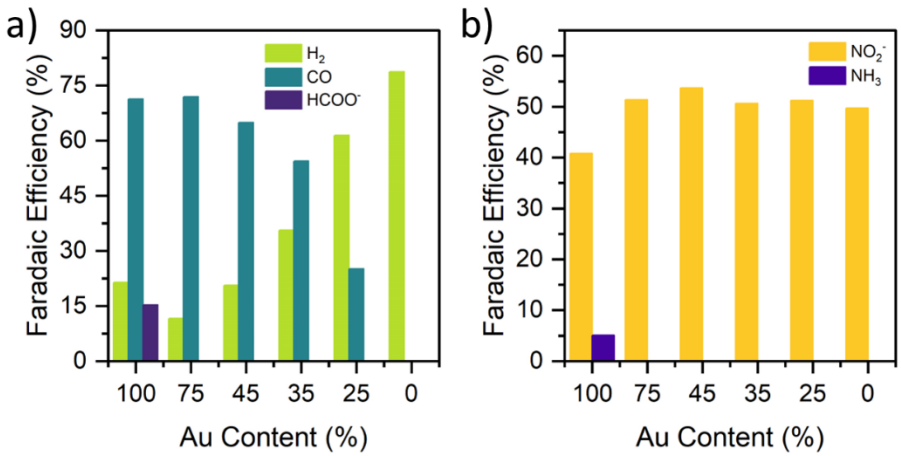

Figure S16. Electrolysis of AuCu alloys and their parent metals at -1 mA cm^{-2} under (a) CO_2RR (0.1 M $KClO_4$, pH = 3.5) and (b) NO_3^-RR control conditions (0.1 M KNO_3, pH = 3.5).

a)

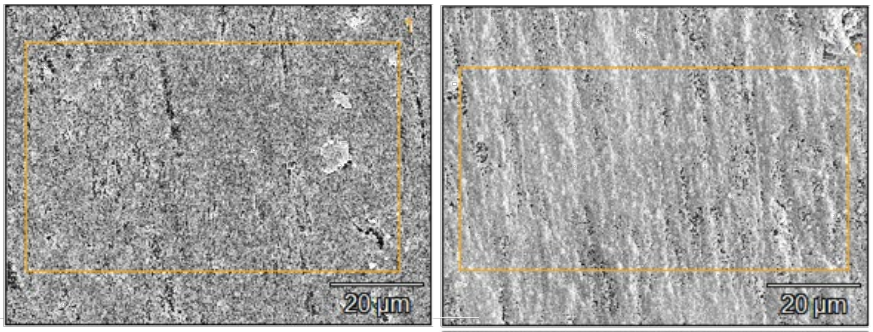

b)

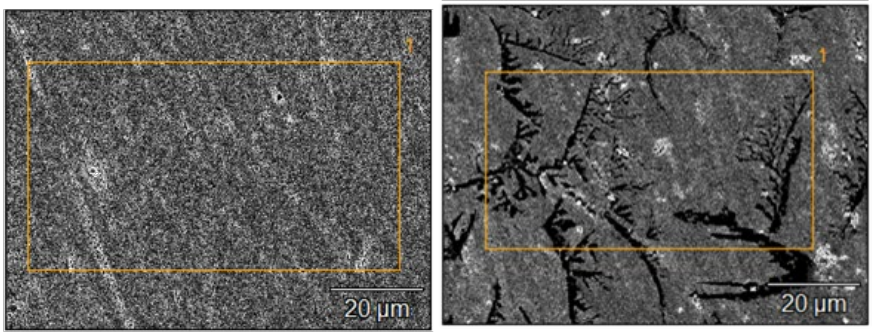

c)

Sample Identity	Atom % Au via EDS	Atom % Cu via EDS
$Au_{75}Cu_{25}$	75.98 (75.6)	24.02 (24.4)
$Au_{25}Cu_{75}$	28.4 (37.52)	71.6 (62.48)

Figure S17: Scanning Electron Micrographs of the highest and lowest Au containing alloys (a) $Au_{75}Cu_{25}$ and (b) $Au_{25}Cu_{75}$ before (left) and after (right) electrolysis at -0.5 mA cm^{-2}. The tabulated data (c) shows the elemental composition of the films, via EDS, before and after (in parentheses) electrolysis. Conditions: 0.1 M KNO_3, pH = 3.5, under sparging CO_2.

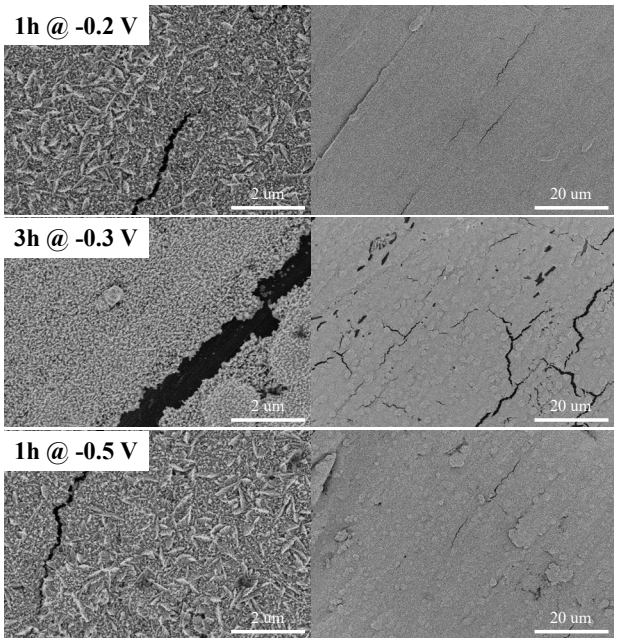

Figure S18. Scanning electron micrographs of the $Au_{75}Cu_{25}$ films following electrolysis at -0.2, -0.3 and -0.5 V vs. RHE. Conditions: 0.1 M KNO_3, pH = 3.5, under sparging CO_2.

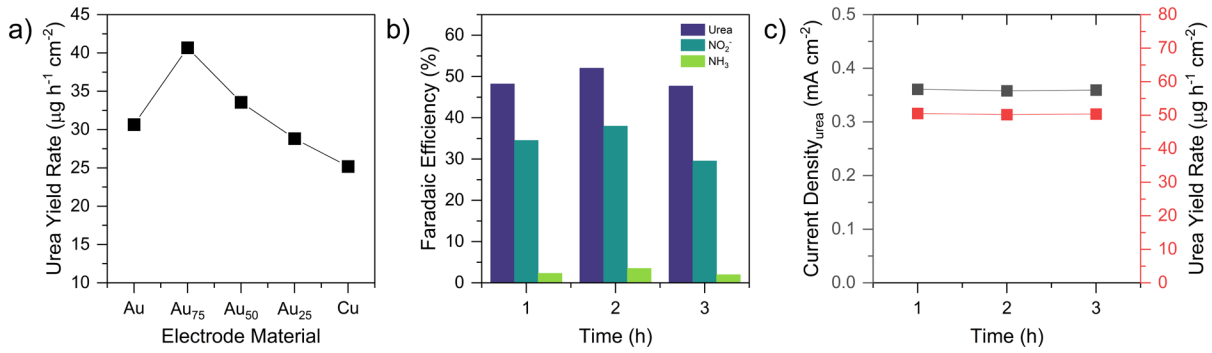

Figure S19. (a) Yield rate for CPE at 0.5 mA for the five electrode materials presented in figure S14. (b) Product distributions following electrolysis at -0.3 V vs. RHE using the $Au_{75}Cu_{25}$ film catalyst in a CO_2-sparged solution of 0.1 M KNO_3, pH = 3.5. Electrolyte was removed and replaced following each 1-hour time point. (c) Activity and yield rates for the 3h electrolysis.

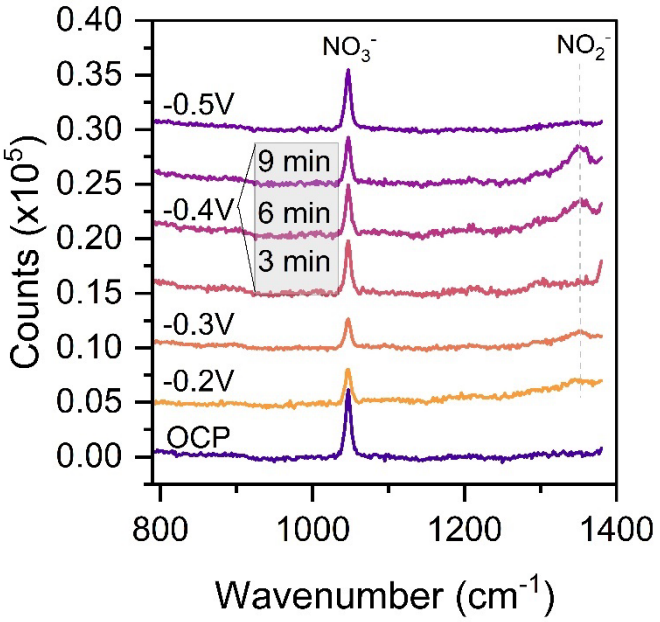

Figure S20. *In situ* Raman spectroscopy of the $Au_{75}Cu_{25}$ film catalyst in 0.1 M KNO_3 (freshly sparged with CO_2, pH = 3.5) at various potentials.

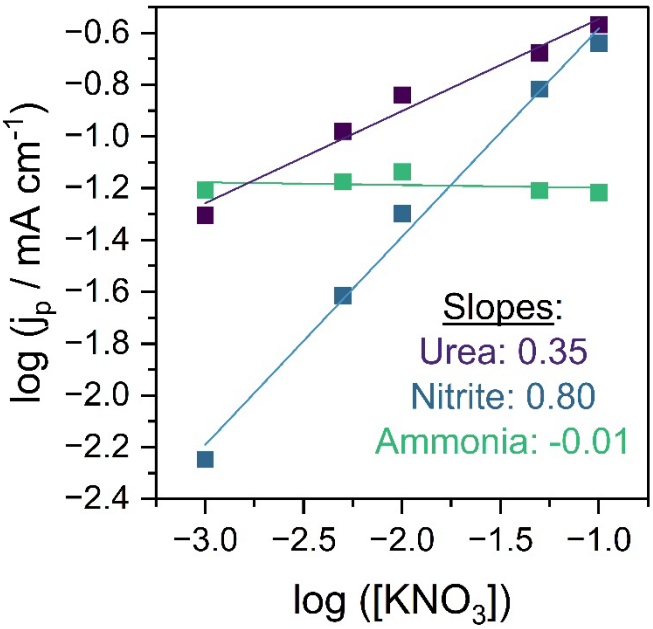

Figure S21. Rate-order determination following batch electrolysis with different concentrations of nitrate in the electrolyte. Conditions: -0.3 V vs. RHE, 0.1 M KNO_3/K_2SO_4, pH = 3.5, under sparging CO_2. K_2SO_4 was used to substitute KNO_3 to maintain ionic strength in the bulk electrolyte.

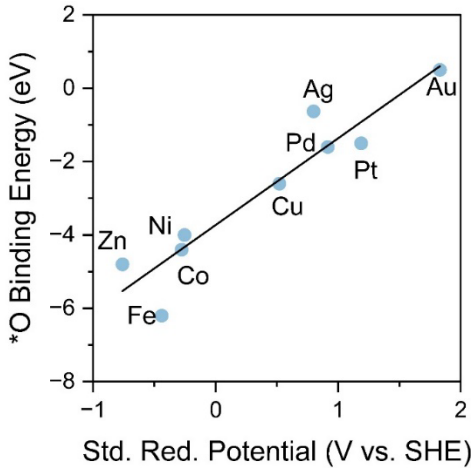

Figure S22. Correlation of metal-oxygen binding affinity and standard reduction potential. Computational binding energy values were obtained from the SUNCAT website[1] and standard reduction potentials were obtained from the Bard electrochemistry textbook[2].

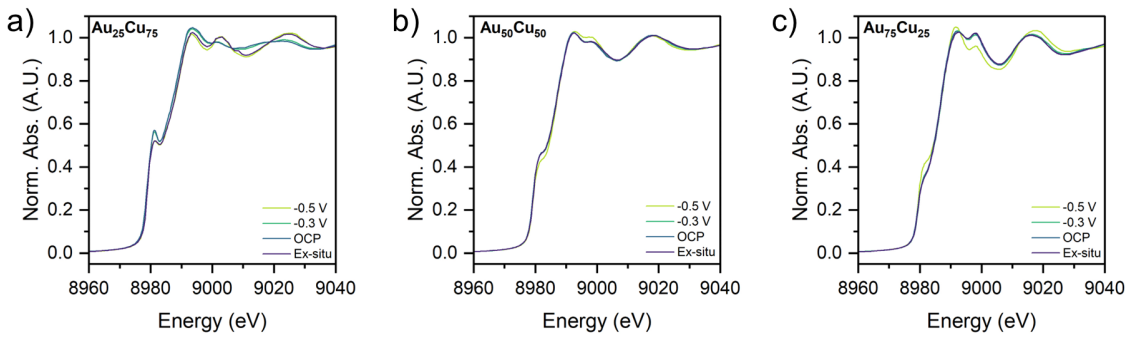

Figure S23. Cu K-Edge XANES Spectra for (a) $Au_{25}Cu_{75}$, (b) $Au_{50}Cu_{50}$, and $Au_{75}Cu_{25}$ (c) alloys under in-situ potential bias. OCP, -0.3 V, -and -0.5 V biases were applied in an electrolyte of 0.1 M KNO_3 constantly purged with CO_2.

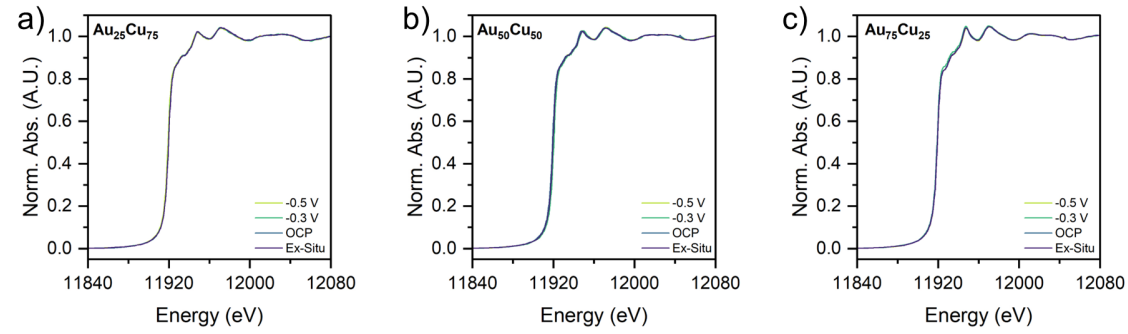

Figure S24. Au L_3-Edge XANES Spectra for (a) $Au_{25}Cu_{75}$, (b) $Au_{50}Cu_{50}$, and $Au_{75}Cu_{25}$ (c) alloys under in-situ potential bias. OCP, -0.3 V, -and -0.5 V biases were applied in an electrolyte of 0.1 M KNO_3 constantly purged with CO_2.

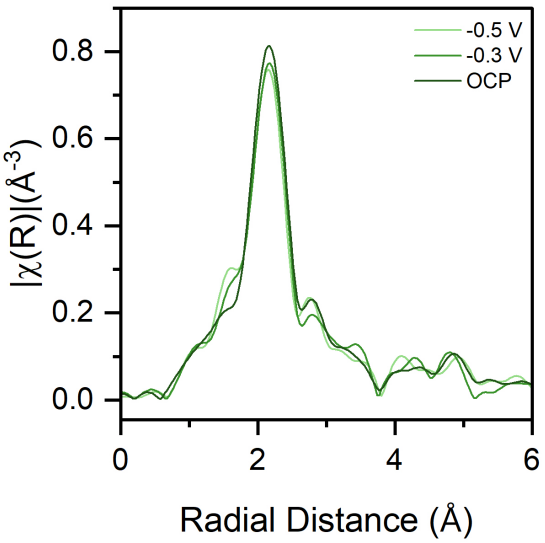

Figure S25. Cu K-Edge EXAFS Spectra for the $Au_{50}Cu_{50}$ alloy under in-situ potential bias. OCP, -0.3 V, -and -0.5 V biases were applied in an electrolyte of 0.1 M KNO_3 constantly purged with CO_2.

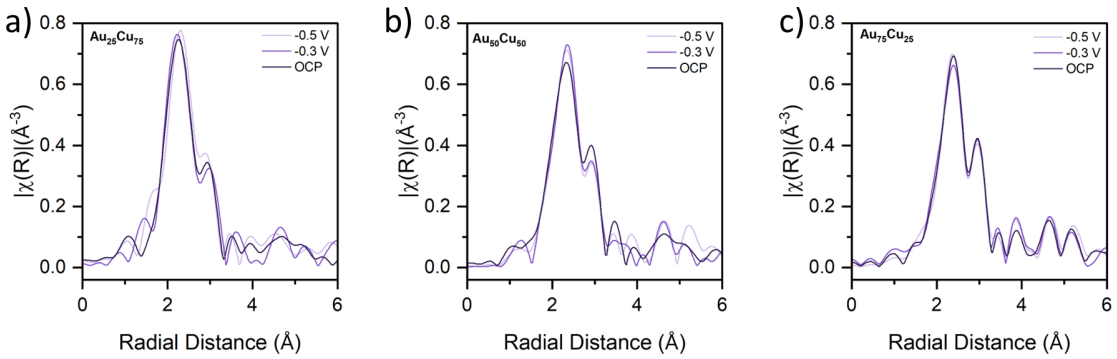

Figure S26. Au L_3-Edge EXAFS Spectra for (a) $Au_{25}Cu_{75}$, (b) $Au_{50}Cu_{50}$, and $Au_{75}Cu_{25}$ (c) alloys under in-situ potential bias. OCP, -0.3 V, -and -0.5 V biases were applied in an electrolyte of 0.1 M KNO_3 constantly purged with CO_2.

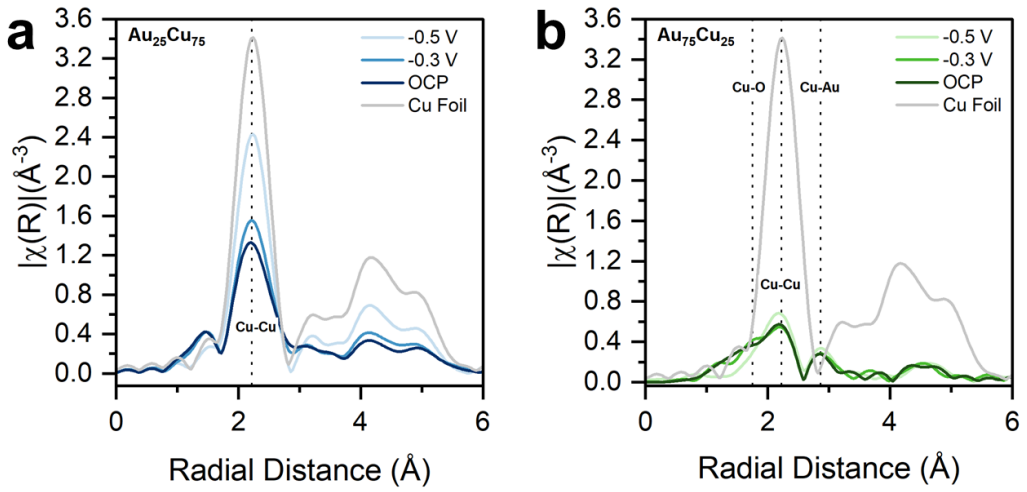

Figure S27. *In situ* Cu K-Edge EXAFS Spectra for the (a) $Au_{25}Cu_{75}$ and (b) $Au_{75}Cu_{25}$ alloy electrodes under a potential bias of OCP, -0.3 V, and -0.5 V vs. RHE with Cu foil reference. Conditions: 0.1 M KNO_3 constantly purged with CO_2.

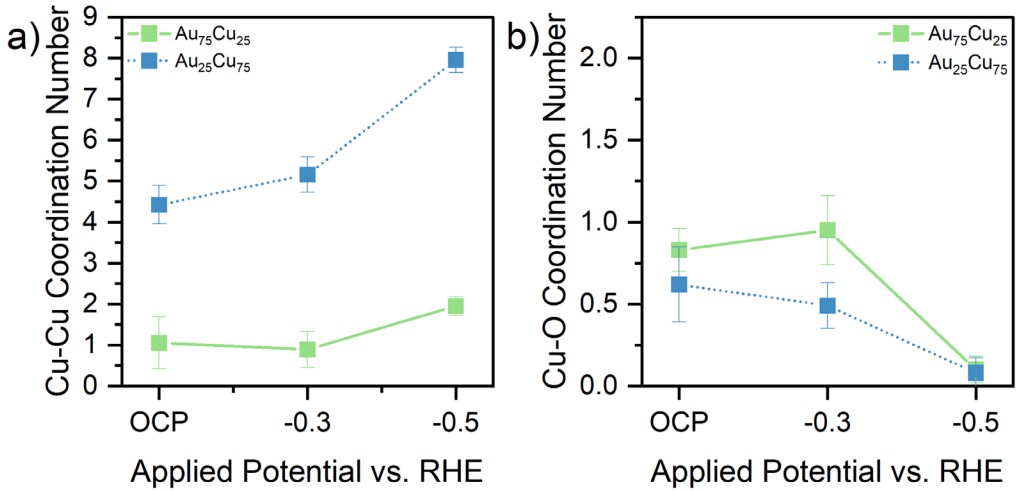

Figure S28. Cu-Cu coordination (a) Cu-O coordination (b) trends from *in-situ* XAS fittings of the $Au_{75}Cu_{25}$ and $Au_{25}Cu_{75}$ alloys. Conditions: 0.1 M KNO_3 constantly purged with CO_2.

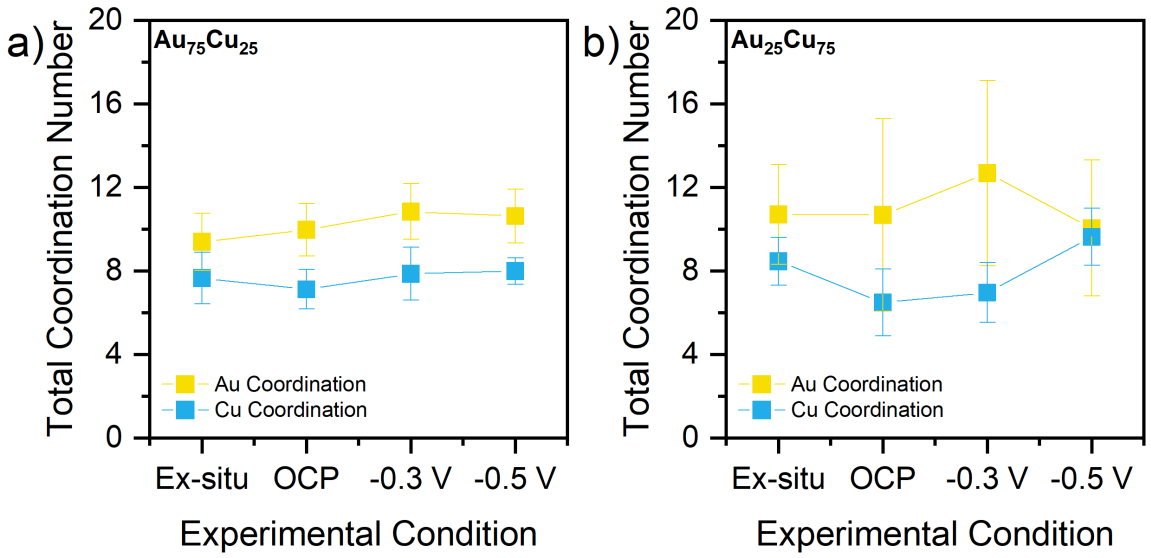

Figure S29. Overall Cu coordination and Au coordination numbers in the (a) $Au_{75}Cu_{25}$ (b) $Au_{25}Cu_{75}$ alloys as a function of potential. Conditions: 0.1 M KNO_3 constantly purged with CO_2.

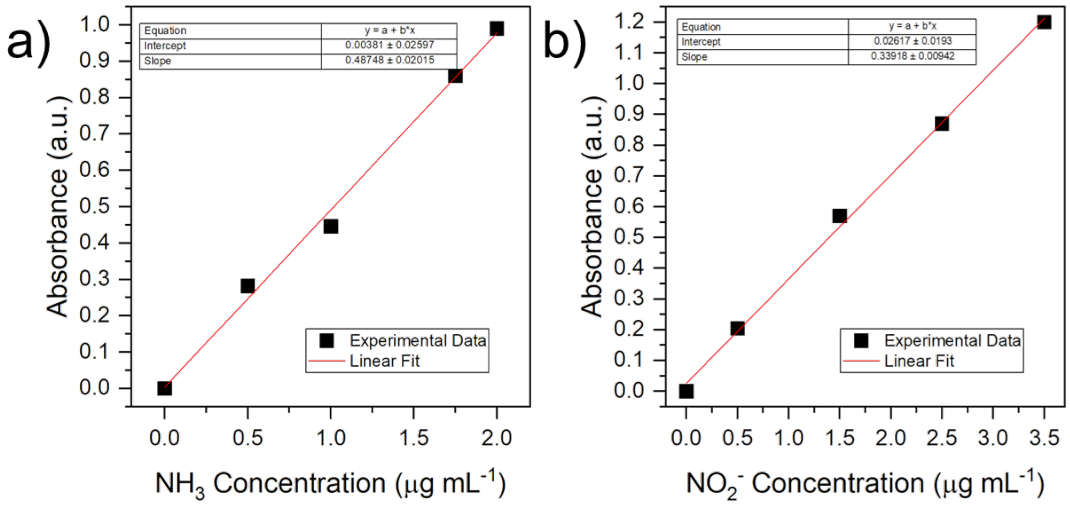

Figure S30. Calibration curves for (a) ammonia and (b) nitrite detection.

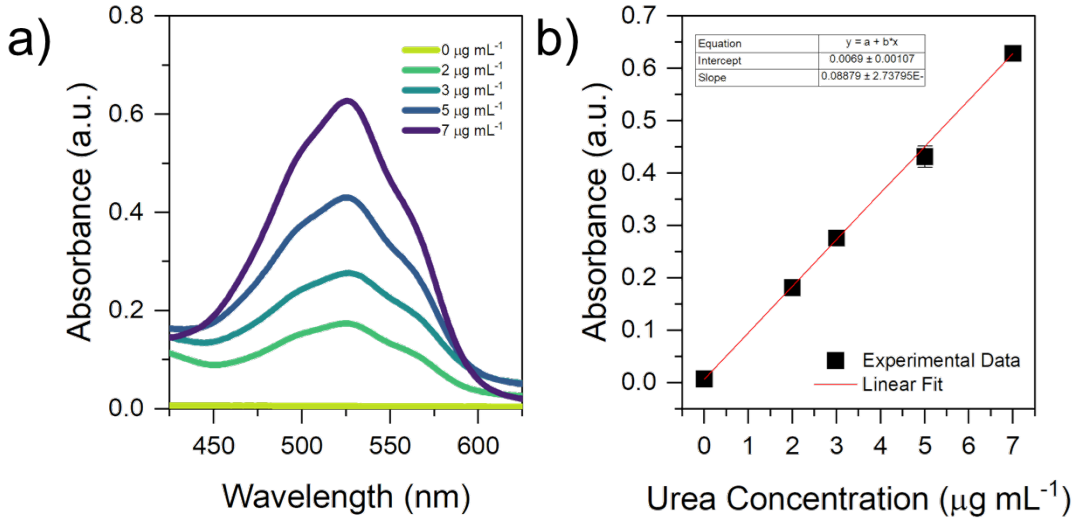

Figure S31. Urea calibration plot. (a) Representative Uv-Vis plot for the diacetyl derivatization and (b) linear fit calibration plot for three independent colorimetric experiments (error bars shown).

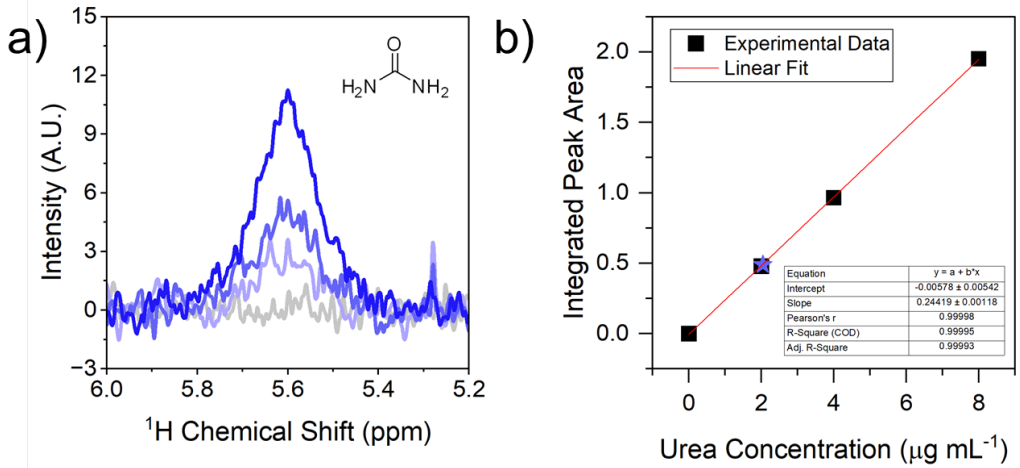

Figure S32. ^{1}H NMR Urea calibration plot. (a) NMR spectra for the calibration samples and (b) linear fit calibration plot. The blue star represents the experimental sample taken after electrolysis for 1 h at -0.3 V vs. RHE in 0.1 M KNO_3, pH = 3.5, under sparging CO_2.

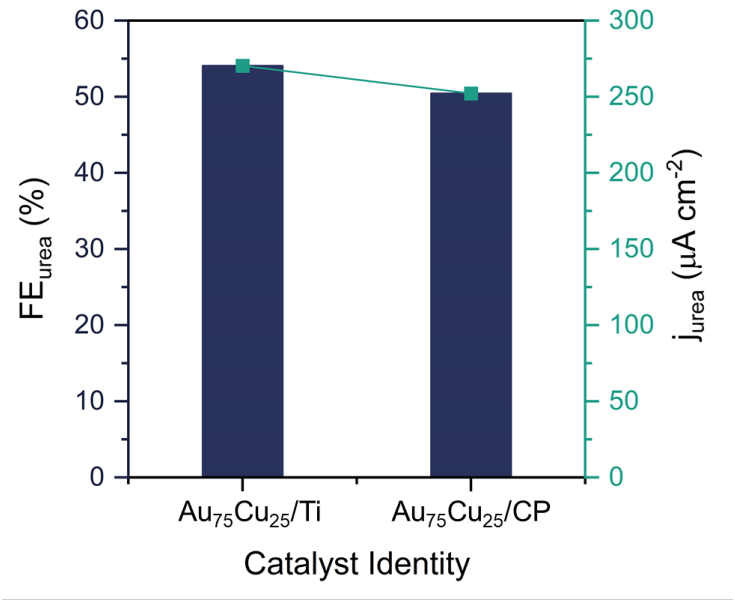

Figure S33. Bulk electrolysis comparison for the $Au_{75}Cu_{25}$ electrode composite at -0.3 V vs. RHE when deposited on either titanium foil or carbon paper. Conditions: 0.1 M KNO_3, pH = 3.5, under sparging CO_2

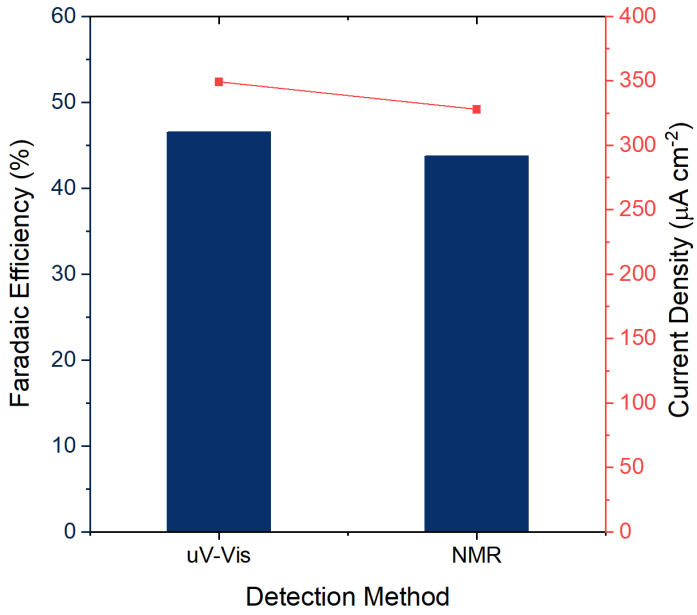

Figure S34. Comparison plot between the colorimetric and NMR detection methods for Urea production. Conditions: -0.3 V vs. RHE, 0.1 M KNO_3, pH = 3.5, under sparging CO_2.

References:

[1] Hummelshøj, J. S.; Abild-Pedersen, F.; Studt, F.; Bligaard, T.; Nørskov, J. K. *Angew. Chemie - Int. Ed*. **2012**, *51*, 272–274. doi: 10.1002/anie.201107947

[2] Bard, A.; Faulkner, L. Electrochemical Methods: Fundamentals and Applications; 2nd ed.; John Wiley & Sons, Inc.: New York, NY, 2002.

[3] B. Ravel and M. Newville, ATHENA, ARTEMIS, HEPHAESTUS: data analysis for X-ray absorption spectroscopy using IFEFFIT, *Journal of Synchrotron Radiation* **2005**, 12, 537–541 doi:10.1107/S0909049505012719

[4] Jain, A.; Ong, S. P.; Hautier, G.; Chen, W.; Richards, W. D.; Dacek, S.; Cholia, S.; Gunter, D.; Skinner, D.; Ceder, G.; Persson, K. A. Commentary: The Materials Project: A materials genome approach to accelerating materials innovation. *APL Materials* **2013**, *1*, 011002. https://doi.org/10.1063/1.4812323